A Segmentation based CFAR Detection Algorithm using Truncated Statistics

Ding Tao, Anthony P. Doulgeris, *Member, IEEE*, and Camilla Brekke, *Member, IEEE*

***Abstract*—Target detection in non-homogeneous sea clutter environments is a complex and challenging task due to the *capture effect* from interfering outliers and the *clutter edge* effect from background intensity transitions. For synthetic aperture radar (SAR) measurements, those issues are commonly caused by multiple targets and meteorological and oceanographic phenomena, respectively. This paper proposes a segmentation based constant false alarm rate (CFAR) detection algorithm using truncated statistics (TS) for multi-looked intensity (MLI) SAR imagery, that simultaneously addresses both issues. From our previous study [1], TS is an useful tool when the region of interest (ROI) is contaminated by multiple non-clutter pixels. Within each ROI confined by the reference window, the proposed scheme implements an automatic image segmentation algorithm, which performs a finite mixture model estimation with a modified expectation maximization (EM) algorithm [2], [3]. Data truncation is applied here to exclude all possible statistically interfering classes, and the sample modeling is based upon the truncated two-parameter gamma model. Next, the CFAR detection is conducted pixel by pixel, utilizing the statistical information obtained from the segmentation process within the local reference window. The segmentation based CFAR detection scheme is examined with real Radarsat-2 MLI SAR imagery. Compared to the conventional CFAR detection approaches, our proposal provides improved background clutter modeling and robust detection performance in non-homogeneous clutter environments.**

***Index Terms*—Target Detection, CFAR, Segmentation, EM algorithm, Truncated Statistics, Non-homogeneous, Modeling, Synthetic Aperture Radar, Sea Clutter.**

I. Introduction

SYNTHETIC aperture radar (SAR) has been exploited for many remote sensing applications, because of its capability of producing Earth surface imagery in all weather conditions, independent of daylight. Maritime target detection, as an important part of monitoring and navigation operations, has attracted much attention for both civil and military purposes over the years. In particular, the popular constant false alarm rate (CFAR) detector adaptively determines the detection threshold while maintaining a certain number of false alarms. Note that its performance is strongly relying on the accurate statistical modeling of the local background clutter measurements. Therefore, characterization of sea clutter becomes a primary procedure for maritime target detection. In an operational context, amplitude or intensity data formats that are multi-looked for the purpose of speckle reduction are conventionally used for ship detection. Hence, in this study, we focus on multi-looked intensity (MLI) SAR imagery. Note that our studied detection algorithm is able to work with single-look complex (SLC) imagery, while the statistics assumptions need to be modified accordingly.

Pixel-wise statistical analysis of the sea clutter has been widely studied in recent years [4]–[9]. With the presence of speckle and other operational conditions (e.g., incidence angle, polarization, etc.), many statistical models have been proposed to represent SAR intensity measurements, such as the gamma, Weibull, $\mathcal{K}$, and $\mathcal{G}^0$ distribution. Note that the $\mathcal{K}$-distribution [4], [5] and $\mathcal{G}^0$-distribution [8] are members of the product model [5]–[7], which describes the backscattered signal as the product between a Gaussian speckle noise-like component and the textured surface mean reflectivity [3], under certain conditions. Note that the probability density function (PDF) of such a product model is often complicated to evaluate and may need numerical integration [3], [10]. A CFAR detector can be derived based on the hypothesized model, while the associate parameters are estimated from the local background clutter using the sliding window technique.

In practice, even with a homogeneous background, the sea clutter confined by the conventional sliding window is often contaminated [1], [11]. One common source of contamination is multiple interfering targets, which usually occurs in dense target situations, such as busy shipping lines, offshore oil/gas production sites and crowded harbors. When there are one or more unwanted outliers in the local reference window in the form of man-made targets and their side-lobes, or ghosts, it inevitably leads to inaccurate parameter estimation and deceptive statistical modeling. Thus the observed probability of false alarms drops below the specified value, and there is a severe degradation of the CFAR detection performance [1], [12, Ch. 14]. This target detection issue is generally known as the *capture effect* [13]–[16].

Many previous studies suggest that the direct solution is to remove the outliers from the local background samples, which is usually achieved by data ranking and censoring with different restrictions [1]. In particular, there are the spatial sub-setting schemes, such as the smallest-of CFAR (SO-CFAR) detector [17] and the variability index CFAR (VI-CFAR) detector [18], the radiometric sub-setting schemes, such as the ordered statistic CFAR (OS-CFAR) detector [19] and the trimmed mean CFAR (TM-CFAR) detector [20], [21], the iterative censoring (IC) scheme [22]–[24], and many hybrid CFAR detectors [15], [16], [25]–[30]. It's worth noting that the data

Ding Tao, Anthony P. Doulgeris, and Camilla Brekke are with the Department of Physics and Technology, University of Tromsø – The Arctic University of Norway.

E-mail: {tao.ding; anthony.p.doulgeris; camilla.brekke}@uit.no

Manuscript received Jan. 5, 2015; revised Jun. 15, 2015; revised Nov. 17, 2015.

0000–0000/00$00.00 © 2015 IEEE

censoring excludes both the interfering targets and naturally occurring bright pixels in the sea clutter, but the remaining samples are not always modeled in a statistically rigorous manner [1]. Although the additional iterative processing in the IC approach improves the censoring results, it generally requires many cycles and long calculation time. On the other hand, by rank-ordering the reference pixels, the OS-based schemes represent the local statistics by a certain value which is less influenced by the outliers, but it suffers performance loss in homogeneous clutter and comes at a higher computational cost [31]. This target detection issue has been addressed in our earlier study of the truncated statistics CFAR (TS-CFAR) [1], where data truncation is implemented to eliminate all possible statistical outliers, and the associated truncated statistics (TS) are utilized for rigorous clutter modeling. We have demonstrated and concluded that the TS is useful and robust in various cases, and its application is preferred in the multiple target situations. Therefore, in this study, we carry on to develop the improved CFAR detection algorithm using the TS.

As a further complication, there are various sea surface features resulting in non-homogeneous clutter [32], e.g., transitions between regions with different wind conditions, low wind spiral marks, backscattering variations due to bathymetry, ship wake presences, etc. They are considered to be responsible for the *clutter edge* effect, which can be described as any form of background intensity transition due to meteorological and oceanographic phenomena. This issue is frequently encountered in target detection within a region of interest (ROI), which causes a rising number of false alarms and lowers the reliability of a fully automatic detection result [32]. In such complicated cases, a single sophisticated model may not be flexible and adaptable enough to incorporate all the variations within the ROI. Thus, the spatial sub-setting strategy has traditionally been applied to obtain a better representation of the local statistics [1], where the subset of the reference samples is selected by the greatest-of (GO) [33] or a function of the current operational environment [18]. Note that, however, many previous studies [18], [20], [33], [34] indicate that such strategy usually suffers inevitable performance degradation and is just suitable for some particular cases.

In recent studies [35]–[37], an improved adaptive sample/region selection stage has been inserted into the algorithm to maintain the CFAR property against difficult background conditions, resulting a two-stage detection scheme. In [35], the heterogeneous secondary data is modeled as a mixture of two different distributions, each with different clutter strengths in the presence of clutter edges. Empirical Bayesian inference is applied in the first stage for training data selection, and an adaptive CFAR detection is conducted next using the identified homogeneous training set regarding the spatial continuity. A similar approach in [37] assumes no more than one clutter edge within the reference window. So the location of the possible edge can be estimated first, and then the CFAR based threshold is calculated using only the region that is more likely to have similar statistics to the cell under test (CUT). Apart from those attempts, the region-growing technique has also been proposed to adaptively optimize the reference region for better false alarm regulation and detection probability, but with an increasing computational cost [36]. In fact, all of the mentioned schemes and attempts are naturally leading towards a general segmentation stage, which obtains the contextual information for the subsequent CFAR detection. This claim also agrees with the main idea in the preliminary studies [32], [38], where an appropriate first segmentation stage allows the standard CFAR techniques to be applied within the homogeneous areas.

In this study, we propose an improved segmentation based CFAR detection algorithm using TS. This paper proceeds to describe the methodology details in Section II. The statistical modeling of non-homogeneous sea clutter is evaluated in Section III, followed by detection performance investigation and discussion in Section IV. All the experiments in this paper are based on real Radarsat-2 SAR imagery. Table I lists the product details of the SAR images applied. Finally, Section V presents the main conclusions and perspectives.

II. METHODOLOGY

The workflow of the proposed segmentation based CFAR detector is shown in Fig. 1. There are three core processors involved, i.e., the pre-processor, the segmentation processor, and the CFAR processor, which are described sequentially in this section.

A. Pre-processor

The process begins with an input MLI image, which could be a ROI of any size as long as it contains sufficient amount of reference pixels for the statistical modeling. In contrast, for most conventional CFAR detectors, a small number of samples outside a guarding area around the CUT is often applied as the detector input [9], due to the increasing risk of non-stationary statistics and *capture effect*. This kind of traditional scheme, which is usually associated with the pixel-wise sliding window technique, is defective in complicated conditions, and inefficient and time-consuming in general, whereas our proposed method does not have such problems.

From our previous study [1], interfering targets often lead to inaccurate parameter estimation and deceptive modeling, hence it is beneficial to integrate the TS from the beginning. As a result, data truncation is the essential operation of the pre-processor. The truncation ratio R_t is defined as the fraction of truncated samples relative to the total number of pixels within the ROI. The value of R_t is determined by the total sample size N_{ROI} and the empirical maximum target size N_{target} in pixels within the ROI and target count c. It is derived as

$$R_t \geq \frac{c \cdot N_{target}}{N_{ROI}} \times 100\% \,. \tag{1}$$

Note that these parameters are user specified empirical values in practice, and the total number of samples N_{ROI} is set to be at least 1000 as the rule of thumb in this study. Furthermore, it is usually impossible to estimate and determine the exact quantity, size, or category of targets within a certain ROI due to the general lack of knowledge. Therefore, it is better to overestimate R_t, which ensures that all possible contaminations are excluded.

TABLE I
RADARSAT-2 PRODUCT DETAILS.
SGF: SAR GEOREFERENCED FINE PRODUCT (ALSO KNOWN AS PATH IMAGE).

No.	Acquired Date & Region	Beam Mode	Product	Polarization	Nominal Pixel Spacing [Rng × Az] (m)	Incidence Angles [degrees]	No. Looks [Rng × Az]
1	2013-08-08, North Sea	ScanSAR Narrow	SGF	Single HH	25×25	19.5 to 39.6	2×2
2	2012-08-23, North Sea	ScanSAR Narrow	SGF	Single HH	25×25	30.8 to 46.6	2×2
3	2009-09-19, Netherlands offshore	ScanSAR Narrow	SGF	Single HH	25×25	19.5 to 39.5	2×2

Next, there is an optional sub-sampling procedure, which reduces the number of samples being passed to the following processors. It is achieved by simply taking every s^{th} sample in the converted image sample vector. Fewer samples lowers the sensitivity for the clutter estimation of the subsequent procedures, but also dramatically decreases the process time [2], [3].

B. Segmentation processor

An advanced unsupervised segmentation processor is included next in the proposed detector workflow. Our main objective is to obtain a good overall statistical model in non-homogenous sea clutter environments.

Based on previous studies [2], [3], [39], the automatic segmentation process is achieved through a finite mixture model estimated with a modified expectation maximization (EM) algorithm, where a goodness-of-fit (GoF) test allows for the splitting of different classes. Note that this is an iterative method that repeatedly estimates the class posterior probabilities for each sample based on the current parameters and then updates the class parameters using the estimated probabilities. It requires a fixed confidence level, a hypothesized PDF expression for the class model, and no initialization. The initial state and the number of classes are addressed with an automatic strategy by consistently starting as one class and adaptively splitting classes until a statistical criterion is satisfied in the GoF test. When the sub-sampling is applied, the subsequent reconstruction to the whole ROI is achieved with a maximum likelihood classification of every pixel in the entire ROI, given the class parametric models obtained for the sub-sampled segmentation [2].

Although it is not necessary in the proposed workflow, the processor can segment the sample pixels into their most likely classes and produce an optional segmented image, if required.

1) Statistical modeling: Compared to the complex product models, the relatively simple two-parameter gamma distribution is considered in this study for the statistical modeling of the MLI measurements X, whose truncated version can also be derived based on TS [1]. Thus, the individual clutter segment is assumed to be gamma distributed with shape parameter α and mean value μ. Its PDF is defined as

$$p_X(x) = \left(\frac{\alpha}{\mu}\right)^{\alpha} \frac{x^{\alpha-1} e^{-x\alpha/\mu}}{\Gamma(\alpha)} \ , \tag{2}$$

where $\Gamma(a) = \int_0^\infty y^{a-1} e^{-y}\, dy$ is the gamma function, and its cumulative distribution function (CDF) is defined as

$$P_X(x) = \frac{\gamma(\alpha, x\alpha/\mu)}{\Gamma(\alpha)} \tag{3}$$

with the lower incomplete gamma function $\gamma(a,\, b)$ defined as $\int_0^b y^{a-1} e^{-y}\, \mathrm{d}y$. The PDF of $\tilde{X}$, the truncated MLI measurements, becomes

$$p_{\tilde{X}}(x;t) = \begin{cases} \frac{p_X(x)}{P_X(t)} = \left(\frac{\alpha}{\mu}\right)^{\alpha} \frac{x^{\alpha-1} e^{-x\alpha/\mu}}{\gamma(\alpha, t\alpha/\mu)} & ; \quad 0 < x \leq t \\ 0 & ; \quad x > t \end{cases} , \tag{4}$$

where the threshold t is called the *truncation depth*, which is obtained based on the previously derived truncation ratio R_t in equation (1), and the normalization by $P_X(t)$ makes sure that $p_{\tilde{X}}(x;t)$ integrates to one.

In the SAR context [7], the shape parameter α is commonly replaced by the equivalent number of looks (ENL), which is equivalent to the number of independent intensity values averaged per pixel. It is usually lower than the number of looks L used pragmatically in the statistical modeling to account for correlation between the samples in $\{X_i\}_{i=1}^{L}$ [40]. The ENL is commonly estimated from a recognized homogeneous region in a SAR image, where the speckle is fully developed, the contribution of texture is negligible, and the radar cross section is assumed to be constant [7]. Note that the ENL is normally considered a global image constant, hence the presence of texture will lead to underestimation. When the local variability of texture is taken into account and the ENL is estimated locally, it is no longer a constant value but a spatially varying number. In this study, the shape parameter α is estimated from each ROI instead of a global ENL, and this provides a better model for the data by implicitly assimilating some of the texture. This could be justified as a more pragmatic approach, and the resulting kind of distribution is called the relaxed two-parameter gamma distribution [41]. The relaxed modeling is adopted to compensate the texture in the clutter to some extent, without using the complicated product models that are noted to be excessively difficult to formulate with TS.

2) Parameter estimation: The mean and shape parameter estimation for each segmented cluster is achieved with the maximum likelihood (ML) estimator. The likelihood function of the truncated two-parameter gamma distribution is derived

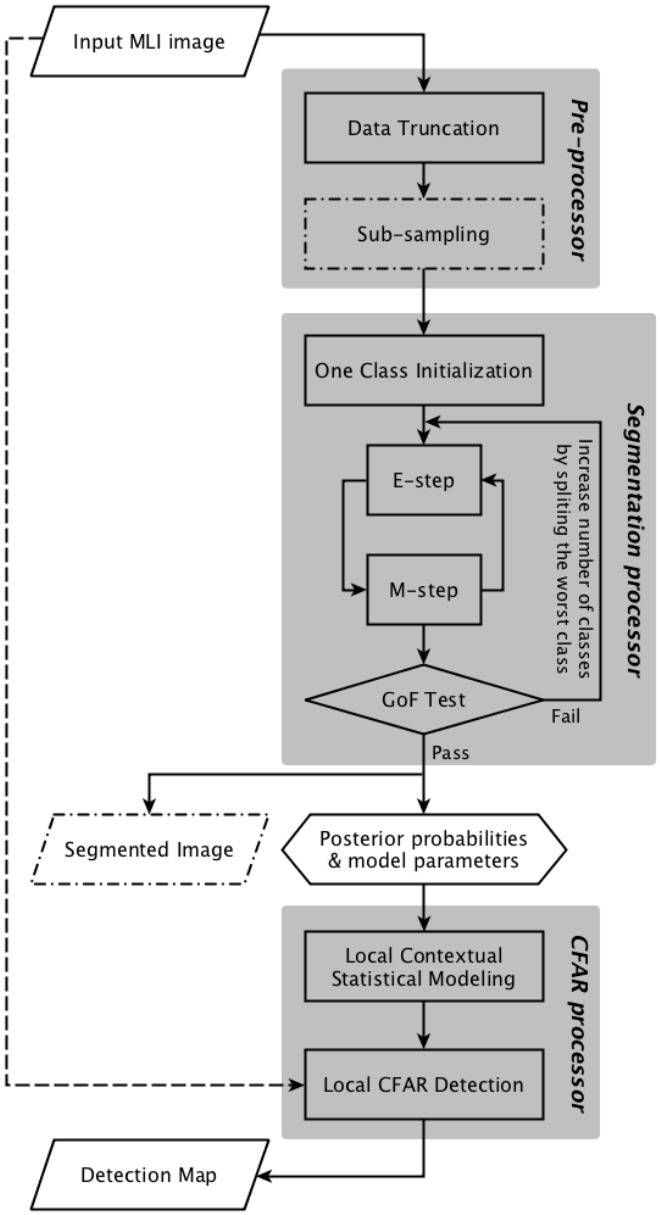

Fig. 1. Workflow of the segmentation based CFAR detector. The solid arrow lines indicate the workflow. The solid parallelograms represent the main input and output. The rectangular boxes show action and procedure in different processors grouped within gray background regions. The diamond is the goodness-of-fit (GoF) test, and the hexagon is internal data passed between processors. Furthermore, the dashed arrow and dot dash line mean additional data path and optional processing procedure and output data, respectively.

as

$$\begin{aligned}\mathcal{L}(\mu,\alpha\,|\,\tilde{\mathbf{x}}) &= \prod_{i=1}^{n} p_{\tilde{X}}(\tilde{x}_i\,|\,\mu,\alpha) \\ &= \Big(\frac{\alpha}{\mu}\Big)^{n\alpha} \frac{e^{-\frac{\alpha}{\mu}\sum_{i=1}^{n}\tilde{x}_i}}{[\gamma(\alpha,\,t\alpha/\mu)]^n} \prod_{i=1}^{n} \tilde{x}_i^{\alpha-1}\ ,\end{aligned} \tag{5}$$

where $\tilde{\mathbf{x}} = [\tilde{x}_1, \ldots, \tilde{x}_n]'$ and $\{\tilde{x}_i\}_{i=1}^{n}$ is a size n sample of truncated MLI measurements. And the log-likelihood function is derived as

$$\begin{aligned}\log \mathcal{L}(\mu,\alpha\,|\,\tilde{\mathbf{x}}) = n\alpha \log\frac{\alpha}{\mu} - n\log\gamma(\alpha,\,t\alpha/\mu) \\ - \frac{n\alpha}{\mu}\frac{1}{n}\sum_{i=1}^{n}\tilde{x}_i \\ + n(\alpha-1)\frac{1}{n}\sum_{i=1}^{n}\log(\tilde{x}_i)\ ,\end{aligned} \tag{6}$$

where $\frac{1}{n}\sum_{i=1}^{n}\tilde{x}_i$ and $\frac{1}{n}\sum_{i=1}^{n}\log(\tilde{x}_i)$ are sample mean of the original and logarithmic truncated MLI measurements. Note that, in the fuzzy segmentation sense [2], [3], the estimated parameters for each class are optimized based on membership weighted sample mean estimates in equation (6). Thus an ML estimator can be obtained from

$$\{\hat{\mu},\hat{\alpha}\} \subseteq \arg\max_{\mu,\alpha}\{\log\mathcal{L}(\mu,\alpha\,|\,\tilde{\mathbf{x}})\}\ , \tag{7}$$

which must be solved numerically due to the combined parameters μ and α in the incomplete gamma function term.

In addition, there is a physical limitation for the shape parameter estimate $\hat{\alpha}$ based on the SAR MLI measurements. When comparing to the pre-estimated global ENL $\hat{l}$ of the image, $\hat{\alpha}$ must always be smaller or equal to it, such as $\hat{\alpha} \le \hat{l}$, otherwise the mean value needs to be estimated independently, with the shape parameter fixed to the ENL estimate. Hence the ML estimator becomes

$$\{\hat{\mu}\} \subseteq \arg\max_{\mu}\{\log\mathcal{L}(\mu,\hat{l}\,|\,\tilde{\mathbf{x}})\}\ . \tag{8}$$

Note that many ENL estimators have been studied previously, e.g. [7], [40], [42]–[44], but this choice is out of the scope of this study. For simplicity, we select the most common definition of the ENL for SAR intensity measurements in [7, Ch. 4] as

$$\text{ENL} = \frac{(mean)^2}{variance}\ . \tag{9}$$

3) Goodness-of-fit test: From our previous studies [2], [3], an hypothesis test was introduced based upon the goodness of fit of the current class model to the observed data. Given that the assumed model distribution is appropriate, then a poor fitting data must represent a mixture of classes. Thus, that class is split into two and the EM segmentation algorithm continues. The end objective is to determine whether the current number of classes and model parameters could explain the data to the given confidence level [3]. A simple histogram test is used based on the multinomial distribution and Pearson's χ^2 test, where an irregular, equiprobable partition of the data is compared directly to the PDF. The normalized total squared error is asymptotically χ^2 distributed as detailed in standard text books, e.g. [45]. This test is fairly generic and can be easily implemented for our model with numerical inversion directly from the PDF expressions that are used in the EM algorithm.

4) Confidence level check: For the main tuning parameter of the GoF test, Table II indicates the chosen confidence level versus the observed false alarm rate for the Pearson's test, which is a demonstration of the GoF test obtaining the specified confidence levels. The Pearson's test is conducted

TABLE II
CONFIDENCE LEVEL VERSUS MEASURED FALSE ALARM RATE WITH TRUNCATION RATIO $R_t = 10\%, 15\%, 20\%, 25\%$. PEARSON'S TEST WITH 50 BINS AND 3 DEGREES OF FREEDOM, 10^5 REPEATS

	Measured failures [%]			
Confidence level [%]	$R_t = 10\%$	$R_t = 15\%$	$R_t = 20\%$	$R_t = 25\%$
90.0	10.196	10.286	10.150	10.239
95.0	5.019	5.192	5.012	5.140
99.0	0.941	1.013	1.042	1.025
99.9	0.101	0.109	0.111	0.124

with 50 bins and 3 degrees of freedom, and the results are averaged from 10^5 Monte Carlo simulations. Each repetition operates in a simulated ROI of 1024 gamma distributed samples with mean value $\mu = 0.5$ and shape parameter $\alpha = 4$, where the truncation ratios considered are 10%, 15%, 20% and 25% related to the total number of samples. A wide range of parameter values were also tested and all showed this same representative behavior.

C. CFAR processor

After the segmentation processor, the PDF for all samples within the ROI can be described by a finite mixture model, which is shown as

$$f(x) = \sum_{i=1}^{\hat{m}} \hat{\pi}_i f_i(x \,|\, \hat{\mu}_i, \hat{\alpha}_i) \;, \tag{10}$$

where $\hat{m}$ is the number of classes determined through the automatic EM segmentation algorithm in Section II-B, $\hat{\pi}_i$ are the class priors (weights) estimated from the ROI such that $\hat{\pi}_i \geq 0$, $\sum_{i=1}^{\hat{m}} \hat{\pi}_i = 1$, and the $f_i(x \,|\, \hat{\mu}_i, \hat{\alpha}_i)$ are the individual class model PDFs with estimated mean and shape parameter. When assuming a two-parameter gamma distributed clutter, each $f_i(x \,|\, \hat{\mu}_i, \hat{\alpha}_i)$ is equal to $p_X(x \,|\, \hat{\mu}_i, \hat{\alpha}_i)$ from equation (2) and the mixture model CDF is then derived as

$$\begin{aligned} F(x) &= \sum_{i=1}^{\hat{m}} \hat{\pi}_i F_i(x \,|\, \hat{\mu}_i, \hat{\alpha}_i) \\ &= \sum_{i=1}^{\hat{m}} \hat{\pi}_i \frac{\gamma(\hat{\alpha}_i, x\hat{\alpha}_i/\hat{\mu}_i)}{\Gamma(\hat{\alpha}_i)} \;. \end{aligned} \tag{11}$$

In the final procedure, our proposed CFAR processor implements target detection using only the local contextual statistics. It is conducted with a pixel-wise expandable sliding window. A small window size of 3×3 is selected initially, in order to maintain the closest reference samples around the CUT. Note that there may be samples that are excluded (truncated) in the pre-processor, which do not possess the segmentation information. Therefore, in this study, whenever the sliding window contains less than 8 untruncated samples, the window will be automatically expand to a larger size. This is to ensure that there is good amount of reference samples for the local contextual statistical modeling.

Next, the posterior probabilities of the neighboring samples confined by the sliding window are collected to calculate the average class weights in the mixture model. Then, the local contextual mixture model is constructed using the estimated class model parameters from the previous processor and their local contextual priors. Hence, the specified false alarm rate P_{FA}, under the estimated mixture model, can be related to the CDF as

$$\begin{aligned} P_{FA} &= 1 - F(T) \\ &= 1 - \sum_{i=1}^{\hat{m}} \hat{\pi}_{i,j} \frac{\gamma(\hat{\alpha}_i, T\hat{\alpha}_i/\hat{\mu}_i)}{\Gamma(\hat{\alpha}_i)} \;, \end{aligned} \tag{12}$$

where $\hat{\pi}_{i,j}$ is the class weights estimated from the local neighborhood samples $(X_1, X_2, \ldots, X_j)$, and T is the detection threshold that needs to be solved for. Lastly, the actual test pixel value is compared to T.

In addition, it is worth noting that there are also some alternative fast CFAR detection schemes that can be considered using the optional segmented image. Similar to the previous studies [17], [33], the conventional concepts, such as the SO-CFAR and GO-CFAR, can be easily achieved here. In a coarse-level process, the CFAR detection is based on one single class model with the smallest or greatest of the mean estimates within the whole ROI. In a local-level process, by using the sliding window technique, only the local dominant class is selected for the detection. In either way, the process time will be reduced to some extent, but also causing varying degrees of detection performance degradation, compared to the proposed comprehensive detection algorithm.

III. STATISTICAL MODELING OF REAL SEA CLUTTER

In this section, the statistical modeling of the non-homogeneous clutter is evaluated with real MLI SAR imagery. Our comparative study is conducted on three different ROIs selected from the image No.1 in Table I, representing real possible cases when such sample regions are used as the reference for the statistical modeling of the background clutter. For comparison, the sea clutter is modeled with the gamma distribution, $\mathcal{K}$-distribution, and a mixture of gamma distributions, whose parameters are estimated by either the conventional estimators or the TS-based ML estimators.

A. Statistical model and parameter estimation

In total, there are 4 modeling approaches considered here, which are described in the following sub-sections. Note that the statistical modeling approach based on a mixture of gamma distributions using the TS has already been introduced in the proposed segmentation processor in Section II.

1) Gamma distribution with sample mean estimate and global ENL: This is the simplest conventional modeling approach included in the evaluation and discussion. The mean value is averaged from all sample values within the ROI, and the shape parameter is replaced by the global ENL constant of the image. Note that the global ENL value is pre-estimated from a manually selected homogeneous region in the image.

2) Gamma distribution with TS-based mean estimate and global ENL: In our previous study [1], a TS-based ML mean estimator has been proposed, which is derived as equation (8). And the same global ENL estimate is applied here as before. This clutter modeling approach is proved to be very effective, when handling a contaminated situation.

3) $\mathcal{K}$-distribution: The product model has been commonly chosen as an appropriate statistical model for the sea clutter in various scenarios. When a gamma distributed texture variable is assumed, the $\mathcal{K}$-distributed intensity PDF is derived as [7, Ch. 5.4]

$$p(I) = \frac{2}{\Gamma(\hat{l})\Gamma(\hat{\nu})}\left(\frac{\hat{l}\,\hat{\nu}}{\hat{\mu}}\right)^{(\hat{l}+\hat{\nu})/2} \times I^{(\hat{l}+\hat{\nu}-2)/2}\mathcal{K}_{\hat{\nu}-\hat{l}}\left[2\left(\frac{\hat{\nu}\,\hat{l}\,I}{\hat{\mu}}\right)^{1/2}\right], \tag{13}$$

where $\hat{\mu}$ is the sample mean estimate of the ROI, $\hat{l}$ is again the global ENL estimate of the image, and $\hat{\nu}$ is the additional order parameter that needs to be estimated as well. Note that the order parameter indicates the texture condition; the larger (smaller) the order parameter, the lower (higher) the texture variation level. Moment-based methods for order parameter estimation have been studied in [46], [47]. In this study, a method of fractional moments (MoFM) estimator is used for the order parameter estimation, which is based on the r^{th}-order moment expression. It is defined as

$$E\langle I^r\rangle = E\langle I\rangle^r \frac{\Gamma(\hat{l}+r)}{\hat{l}^r\Gamma(\hat{l})}\frac{\Gamma(\nu+r)}{\nu^r\Gamma(\nu)}, \tag{14}$$

where $E\langle\cdot\rangle$ is the expectation operator. Equation (14) is solved numerically for ν with the moment order set to $r = 0.5$ and replacing population moments with sample moments computed from the intensity measurements in the ROI. Another practical solution would be to estimate the model parameters with the method of log-cumulants (MoLC). Although it is not considered in this study for simplicity, the MoLC has shown relatively simple numerical expressions and lower bias and variance compared to moment based methods for product based distributions [48].

B. Result assessment

Fig. 2 to 4 show three case studies with different ROIs selected from the real MLI SAR image No.1 in Table I. The case studies are chosen to demonstrate homogeneous clutter contaminated by multiple interfering targets, uncontaminated non-homogeneous clutter with complex clutter edges, and non-homogeneous clutter with interfering targets, respectively. All ROIs contain the same 9×10^4 number of pixels. For the proposed segmentation based scheme using TS, a 10% truncation ratio is chosen, the confidence level is set to be 99% in the GoF test, and a sub-sampling factor of $s = 4$ is applied.

As shown in Fig. 2(a), there are two targets within the ROI. A reference sample region contaminated by one or more targets is commonly seen in dense target situations. Although, the ROI appears to be mostly homogeneous, our proposed segmentation algorithm is sensitive enough to segment the background into two classes in Fig. 2(b). Note that the truncated pixels are not assigned to any class, as this is not necessary at this stage (shown in black). Fig. 2(c) and 2(d) provide the visual and numerical inspection of the goodness of fits. It is obvious that the conventional statistical modeling approaches, such as the single gamma and $\mathcal{K}$ distribution, are significantly biased by the interfering targets within the region. As a result, excessive heavy tails are observed, which will amplify the threshold calculated at the specified false alarm rate, lower the observed false alarm rate, and increase the risk of missing weak target in the detection. In contrast, by using the TS, the interfering target pixels can be excluded from the reference samples, leading to a better statistical modeling performance. The results clearly show that both TS-based approaches provide good overall fitting to the intensity measurements.

Fig. 3(a) demonstrates another common situation, where the background intensity transitions between different regions yield multiple complex clutter edges. In this case, the proposed segmentation processor is able to properly segment the ROI into two classes, and the clutter edges seems to be well preserved as well. Reflected in the modeling results in Fig. 3(c) and 3(d), the mixture model approach definitely shows the best goodness of fits among others. Although the single $\mathcal{K}$-distributed PDF can take the texture variations into account and fit the data all right, especially for the intensity values above the truncation depth, it is merely by coincidence. As for the single gamma PDFs, they are obviously not suitable for the statistical modeling in the clutter edge situation.

Finally, in Fig. 4, the clutter modeling performance is evaluated in the most challenging case, where both the interfering targets and clutter edges appear in the same ROI. The proposed segmentation algorithm using TS still provides excellent overall model fitting to the data and produces appropriate segmentation results, in spite of all the difficulties. In summary, it is also worth noting that the TS-based modeling approaches show excellent results below the truncation depth, and only diverge above that depth due to the missing information after the data truncation. And towards the higher intensity values, the increasing variances shown in the numerical inspection indicate the histogram estimation error due to very few samples in the tail region of the distributions. In addition, the user specified settings like the confidence level and the degree of sub-sampling of the input image will affect the detail level of the segmentation, revealing only the major classes, or a variable level of detail [2]. In the experiments, a wide range of settings have been investigated before choosing the settings for demonstration. According to the user requirements, a fast coarse level segmentation results can be obtained with a higher

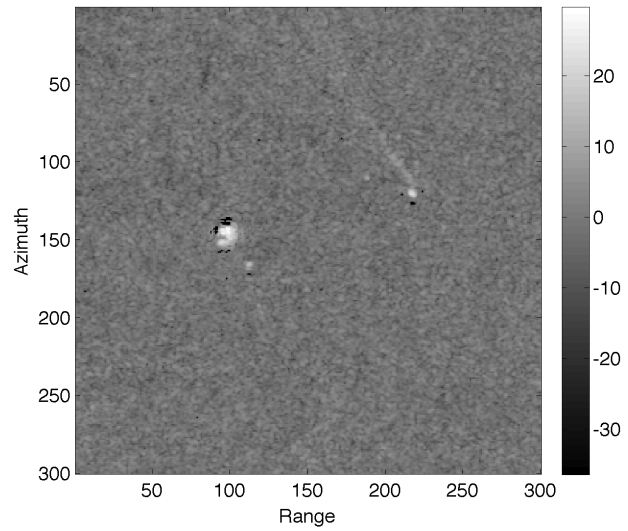

(a) ROI in decibels.

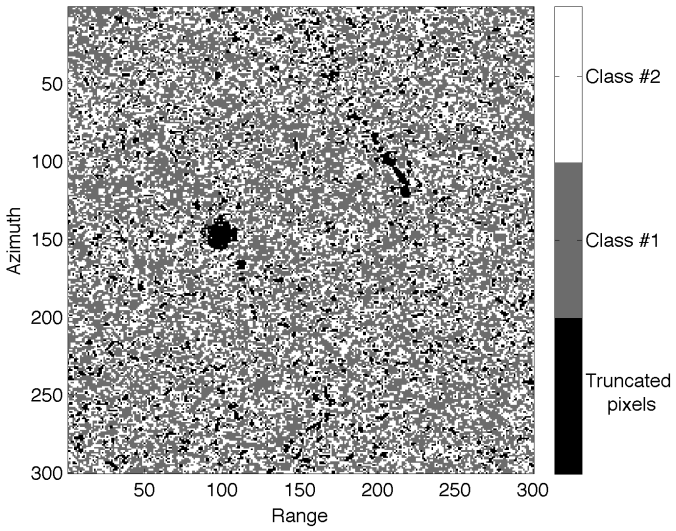

(b) Preliminary segmentation result.

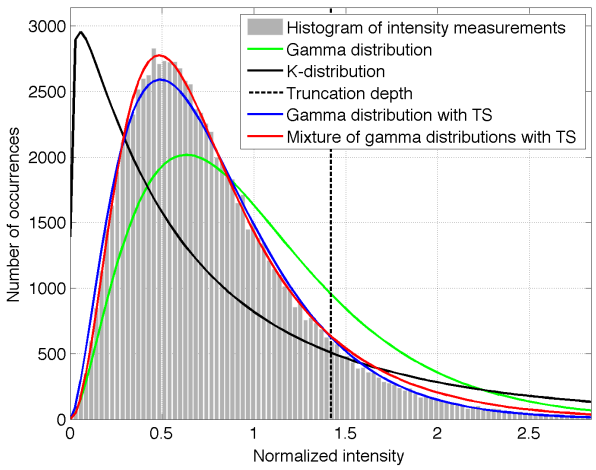

(c) Visual inspection of GoF.

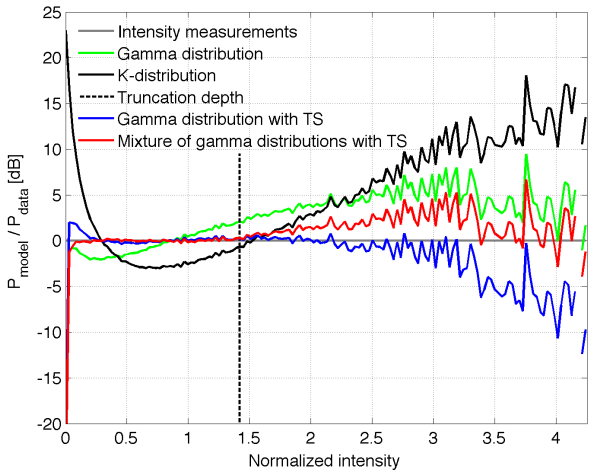

(d) Numerical inspection of GoF.

Fig. 2. Case 1: Comparative analysis of the statistical modeling of real sea clutter. Sub-figures (a) and (b) show the selected ROI from an real MLI HH polarization SAR image and the optional preliminary segmentation result produced by the proposed segmentation processor. The visual inspection of the goodness of fits is presented in sub-figure (c), where different statistical modeling approaches are indicated by distinct colors. The green and black curves are the single gamma and $\mathcal{K}$-distributed PDFs based on the conventional parameter estimates. The blue curve is the single gamma PDF based on the TS-based ML parameter estimates, and the red curve is the PDF of a mixture of two gamma distributions estimated with the TS-based fuzzy ML estimator. Note that all PDFs are scaled to match the histogram of the intensity measurements, and the numerical inspection in sub-figure (d) shows the ratios of the scaled PDFs to the observed histogram in decibels, which is denoted as P_{model}/P_{data}.

confidence level and/or a larger sub-sampling factor, while the opposite for a slow fine level process.

IV. CFAR DETECTION PERFORMANCE

This section examines the proposed segmentation based CFAR detection performance in various real scenarios based on the Radarsat-2 SAR images listed in Table I. A number of different combinations of the user specified settings were evaluated during the experiments, which include different truncation ratios, sub-sampling factors, confidence levels and specified false alarm rates. The essential CFAR properties, such as the false alarm regulation and the detection rate, are considered and assessed in the study.

A. Operational scheme

As mentioned in the previous Section II-A, an MLI SAR image with any size can be accepted as the detector input. For the images covering large areas, a modified stepping window technique is introduced and applied in the experiments, which is sketched in Fig. 5.

As a result, the segmentation window confines the total region that goes into the pre-processor and segmentation processor, and the final CFAR detection is only conducted within the region marked by the detection window. Note that the inner block shifting window goes through the whole image without overlapping, while the outer larger window makes sure the local contextual information for the pixels on the edges of the detection window are collected as well. In this study, the

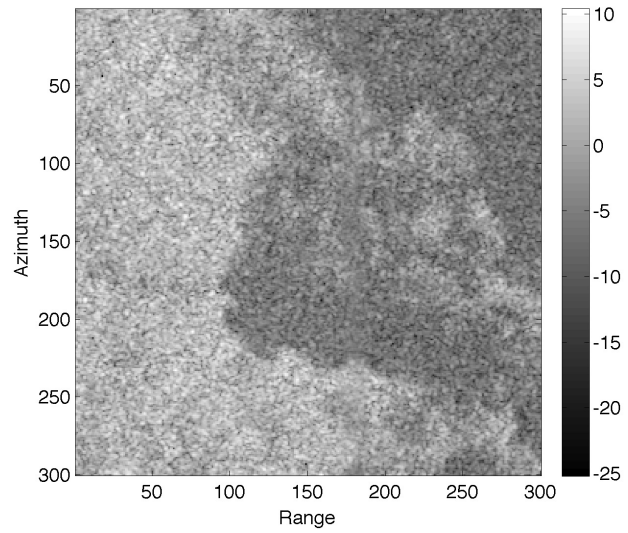

(a) ROI in decibels.

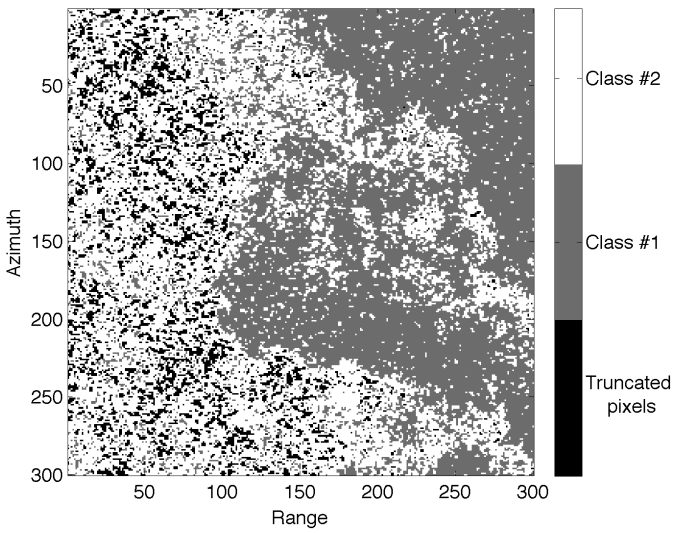

(b) Preliminary segmentation result.

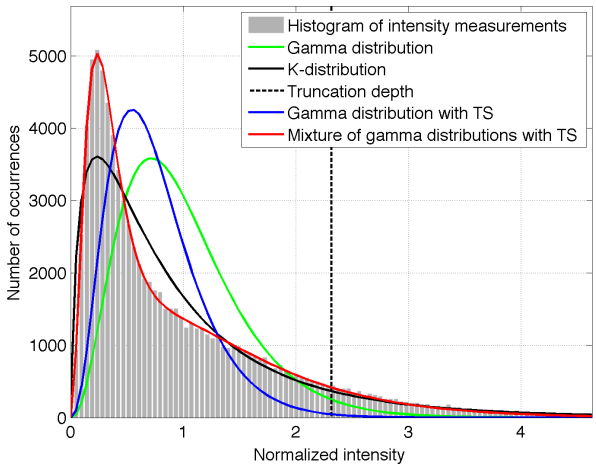

(c) Visual inspection of GoF.

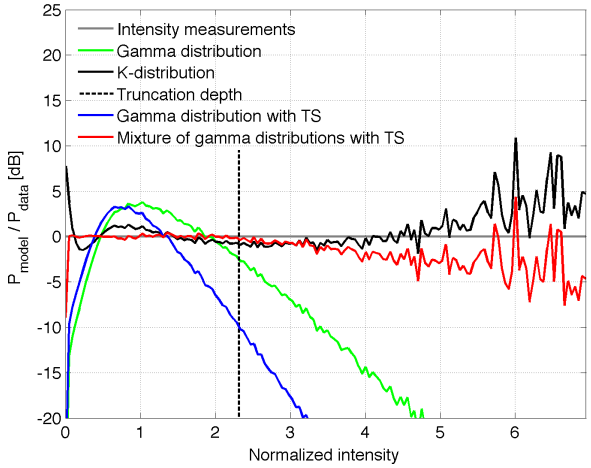

(d) Numerical inspection of GoF.

Fig. 3. Case 2: Comparative analysis of the statistical modeling of real sea clutter. Sub-figures (a) and (b) show the selected ROI from an real MLI HH polarization SAR image and the optional preliminary segmentation result produced by the proposed segmentation processor. The visual inspection of the goodness of fits is presented in sub-figure (c), where different statistical modeling approaches are indicated by distinct colors. The green and black curves are the single gamma and $\mathcal{K}$-distributed PDFs based on the conventional parameter estimates. The blue curve is the single gamma PDF based on the TS-based ML parameter estimates, and the red curve is the PDF of a mixture of two gamma distributions estimated with the TS-based fuzzy ML estimator. Note that all PDFs are scaled to match the histogram of the intensity measurements, and the numerical inspection in sub-figure (d) shows the ratios of the scaled PDFs to the observed histogram in decibels, which is denoted as P_{model}/P_{data}.

segmentation window is designed to double the size of the detection window in both the azimuth and range directions.

B. Result assessment

In Fig. 6 to 9, some selected sub-regions of the original images and the corresponding detection results are demonstrated. Note that many more regions and images have been tested during the experiments, but not included due to limited space. The ground truth is based on visual inspection or automatic information system (AIS) positioning data.

First of all, the detection results shown in this section are obtained with the same user specified settings, i.e., 300×300 pixels detection window, 10% truncation ratio, sub-sampling factor 4, 99% confidence level and 0.001% specified false alarm rate. In addition, many different setting combinations were also evaluated during the experiments. Note that because the chosen settings may not necessarily be the most favorable for each individual image, the adaptivity and robustness of the proposed segmentation based CFAR detector can be well demonstrated.

Fig. 6(a) shows a complex and challenging sea clutter situation for target detection. There are multiple targets appearing in the image. An obvious clutter transition between different sea states is found across the scene. And many cloud-like clutter structures spread over the image. From the detection result in Fig. 6(b), all targets are clearly detected, and there are no excessive false alarms observed around the complex clutter edges. Fig. 7(a) and 8(a) show two sub-regions from another SAR image, where possible oil spills are appeared around

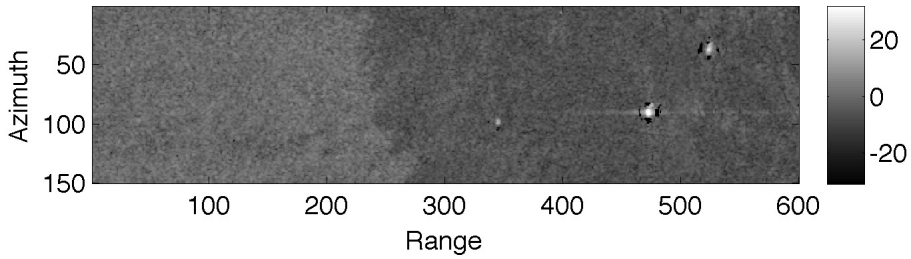

(a) ROI in decibels.

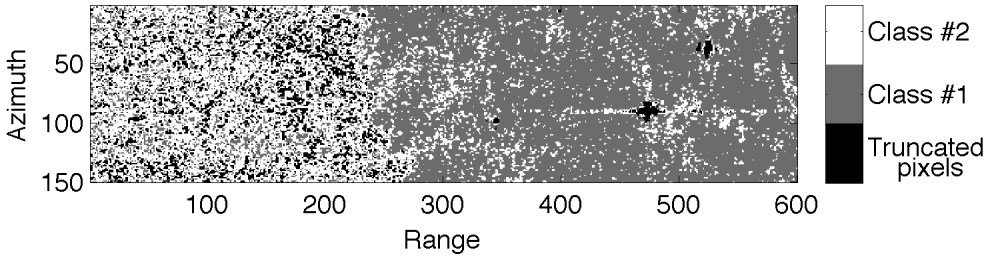

(b) Preliminary segmentation result.

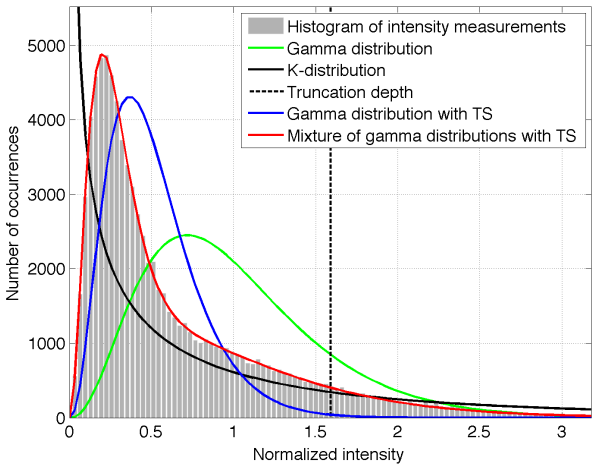

(c) Visual inspection of GoF.

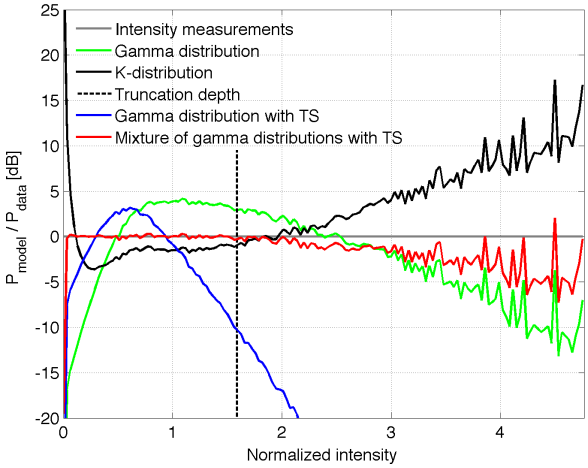

(d) Numerical inspection of GoF.

Fig. 4. Case 3: Comparative analysis of the statistical modeling of real sea clutter. Sub-figures (a) and (b) show the selected ROI from an real MLI HH polarization SAR image and the optional preliminary segmentation result produced by the proposed segmentation processor. The visual inspection of the goodness of fits is presented in sub-figure (c), where different statistical modeling approaches are indicated by distinct colors. The green and black curves are the single gamma and $\mathcal{K}$-distributed PDFs based on the conventional parameter estimates. The blue curve is the single gamma PDF based on the TS-based ML parameter estimates, and the red curve is the PDF of a mixture of two gamma distributions estimated with the TS-based fuzzy ML estimator. Note that all PDFs are scaled to match the histogram of the intensity measurements, and the numerical inspection in sub-figure (d) shows the ratios of the scaled PDFs to the observed histogram in decibels, which is denoted as P_{model}/P_{data}.

the targets, together with few weak targets in the neighboring area at the same time. As shown in Fig. 7(b) and 8(b), good detection results are achieved in both cases, not only for the big bright targets, but also for the small weak ones. In the end, an unusual case is demonstrated in Fig. 9(a), where a wind farm offshore of Netherlands is covered within the SAR image. A large number of wind turbines are located in an extremely close range, while background clutter variations are observed in the same region. It is clear that the proposed detector is able to provide an excellent performance in Fig. 9(b). All targets are detected and can be distinguished individually. The clutter variation effects are suppressed to a minimum as well. Finally, it's worth noting that there are a few excess false alarms observed at the natural sea clutter spikes within the tested images, which are part of the fine clutter structures and considered lookalikes of the targets. It is possible to solve this issue by adjusting the user specified settings.

V. Conclusions

In this paper, we looked into target detection in non-homogeneous sea clutter environments. The frequently encountered issues caused by the capture and clutter edge effects are primarily responsible for the CFAR detection performance degradation resulting in excessive false alarms and/or missing targets. A robust segmentation based CFAR detector using TS has been proposed, where the introduction

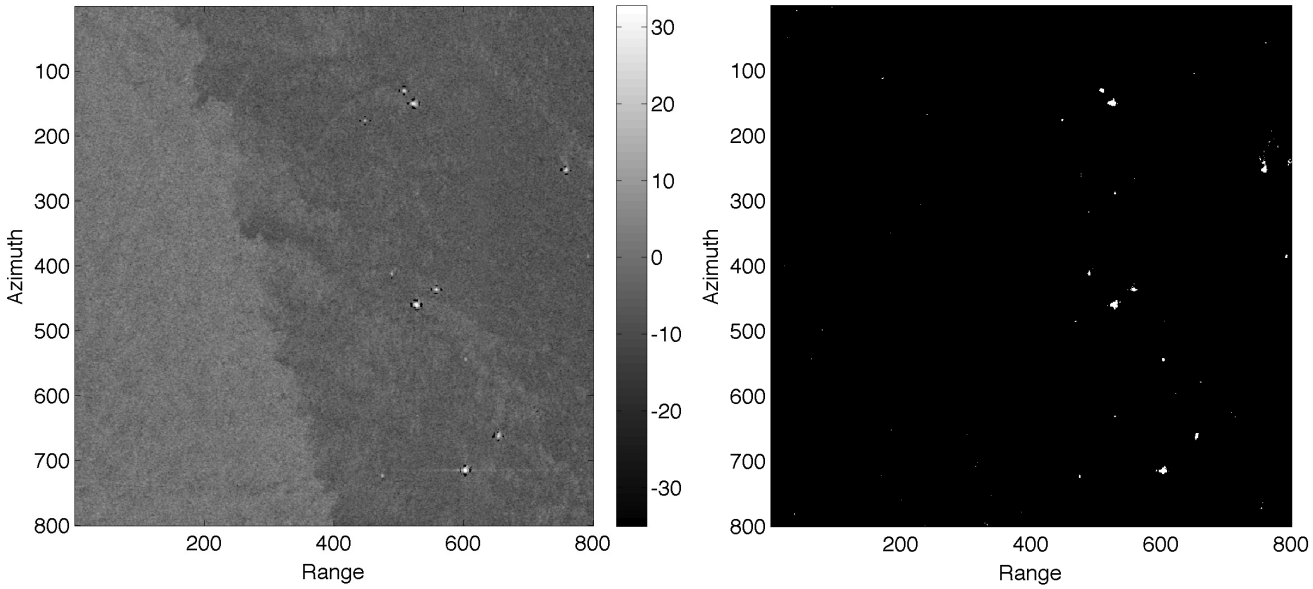

(a) Intensity image in decibels.

(b) Detection result.

Fig. 6. CFAR detection performance study. (a) sub-region of the MLI HH polarization SAR image acquired on 8^{th} August 2013, the North Sea (image No.1 in Table I); (b) detection result obtained with 300×300 pixels detection window, 10% truncation ratio, sub-sampling factor 4, 99% confidence level and 0.001% specified false alarm rate.

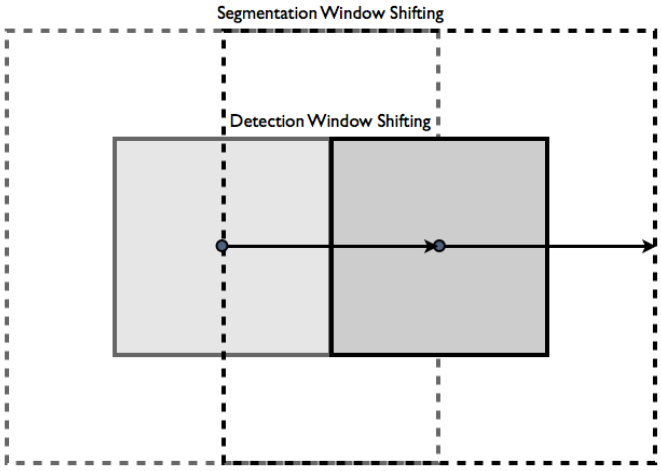

Fig. 5. Stepping window structure of the segmentation based CFAR detector. The solid line rectangle marks the block shifting detection window with no overlap, while the dashed line rectangle indicates the larger segmentation window centralized around the inner detection window.

of the truncated statistics and the segmentation stage have proved to be favorable and beneficial in various real complex situations. The practical performance has been demonstrated in the experiments using real Radarsat-2 MLI SAR images.

Compared with the conventional algorithms, the improved automatic TS based segmentation processor provides a comprehensive statistical analysis of the non-homogeneous background clutter independent from the interfering outliers. The subsequent CFAR processor takes advantage of the available local contextual information, yields a controlled false alarm rate, and achieves excellent detection capability. Thus, the proposed scheme is able to adapt to the complicated target conditions and variations of the background clutter, and is qualified for a robust context-based fully automatic system for sea monitoring under different circumstances by SAR.

Moreover, a multidimensional approach is going to be developed to enhance the target detection performance using multi-polarization SAR data. Additional expansion of the algorithm could also be made by deriving the truncated statistics for other hypothesized sea clutter models, such as the common $\mathcal{K}$ and $\mathcal{G}^0$ distribution.

ACKNOWLEDGMENT

The authors would like to thank Assoc. Prof. Stian Normann Anfinsen at University of Tromsø – The Arctic University of Norway for valuable discussions. This study was partly funded by the Norwegian Research Council through the Arctic Earth Observation and Surveillance Technologies (ArcticEO) project. Radarsat-2 data are provided by Norwegian Space Centre/Kongsberg Satellite Services under the Norwegian–Canadian Radarsat agreement 2013.

REFERENCES

[1] D. Tao, S. Anfinsen, and C. Brekke, "Robust CFAR detector based on truncated statistics in multiple-target situations," *Geoscience and Remote Sensing, IEEE Transactions on*, vol. 54, no. 1, pp. 117–134, Jan. 2016.

[2] A. P. Doulgeris, S. N. Anfinsen, and T. Eltoft, "Automated non-Gaussian clustering of polarimetric synthetic aperture radar images," *Geoscience and Remote Sensing, IEEE Transactions on*, vol. 49, no. 10, pp. 3665–3676, Oct. 2011.

[3] A. P. Doulgeris, "An automatic U-distribution and Markov random field segmentation algorithm for PolSAR images," *Geoscience and Remote Sensing, IEEE Transactions on*, vol. 53, no. 4, Apr. 2015.

[4] E. Jakeman and P. Pusey, "A model for non-Rayleigh sea echo," *Antennas and Propagation, IEEE Transactions on*, vol. 24, no. 6, pp. 806–814, Nov. 1976.

[5] S. H. Yueh, J. A. Kong, J. K. Jao, R. T. Shin, and L. M. Novak, "K-distribution and polarimetric terrain radar clutter," *Journal of Electromagnetic Waves and Applications*, vol. 3, no. 8, pp. 747–768, 1989.

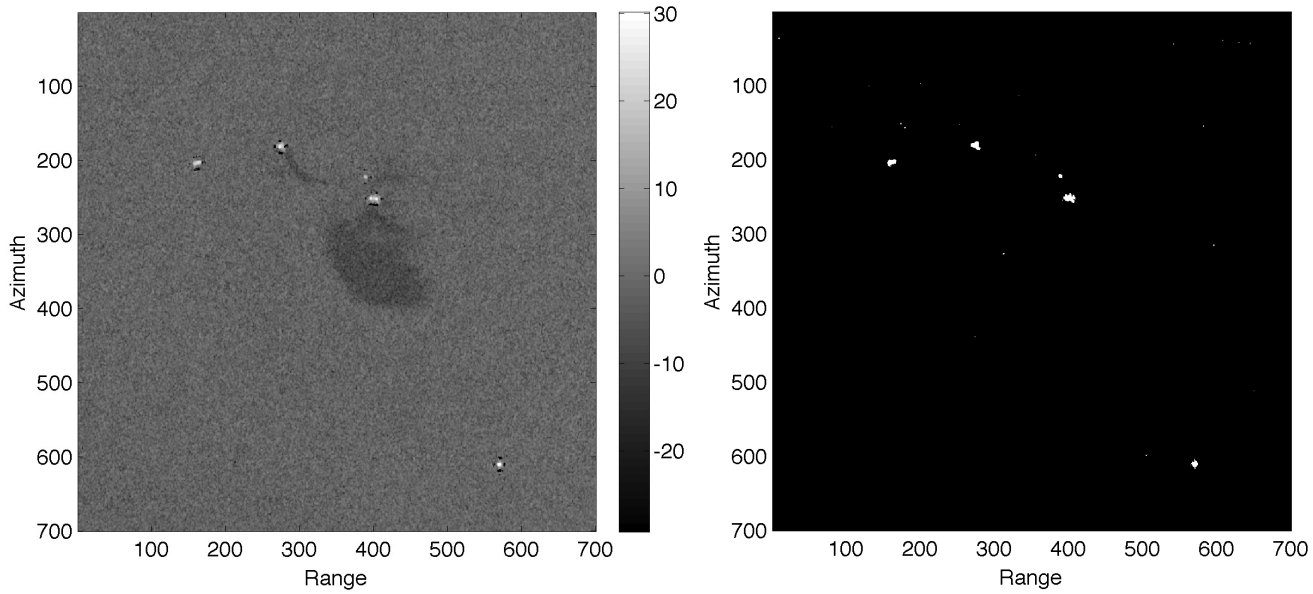

(a) Intensity image in decibels. (b) Detection result.

Fig. 7. CFAR detection performance study. (a) sub-region of the MLI HH polarization SAR image acquired on 23rd August 2012, the North Sea (image No.2 in Table I); (b) detection result obtained with 300×300 pixels detection window, 10% truncation ratio, sub-sampling factor 4, 99% confidence level and 0.001% specified false alarm rate.

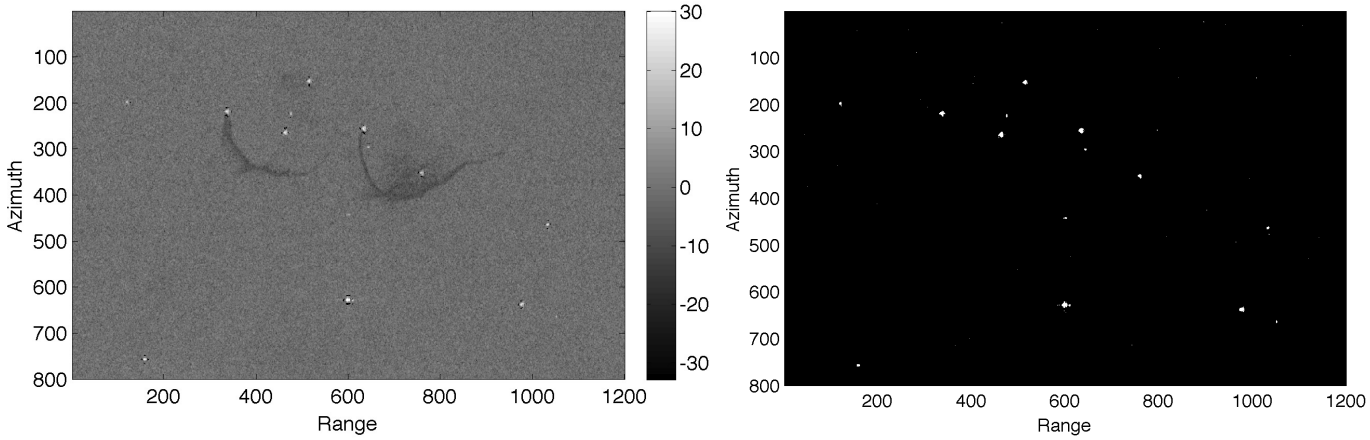

(a) Intensity image in decibels. (b) Detection result.

Fig. 8. CFAR detection performance study. (a) sub-region of the MLI HH polarization SAR image acquired on 23rd August 2012, the North Sea (image No.2 in Table I); (b) detection result obtained with 300×300 pixels detection window, 10% truncation ratio, sub-sampling factor 4, 99% confidence level and 0.001% specified false alarm rate.

[6] S. Yueh, J. Kong, J. Jao, R. Shin, H. Zebker, and T. L. Toan, "K-distribution and multi-frequency polarimetric terrain radar clutter," *Journal of Electromagnetic Waves and Applications*, vol. 5, no. 1, pp. 1–15, 1991.

[7] C. Oliver and S. Quegan, *Understanding Synthetic Aperture Radar Images*, ser. SciTech radar and defense series. SciTech Publ., 2004.

[8] C. C. Freitas, A. C. Frery, and A. H. Correia, "The polarimetric G distribution for SAR data analysis," *Environmetrics*, vol. 16, no. 1, pp. 13–31, 2005. [Online]. Available: http://dx.doi.org/10.1002/env.658

[9] C. Fei, T. Liu, G. Lampropoulos, and V. Anastassopoulos, "Markov chain CFAR detection for polarimetric data using data fusion," *Geoscience and Remote Sensing, IEEE Transactions on*, vol. 50, no. 2, pp. 397–408, Feb. 2012.

[10] S. N. Anfinsen and T. Eltoft, "Application of the matrix-variate Mellin transform to analysis of polarimetric radar images," *Geoscience and Remote Sensing, IEEE Transactions on*, vol. 49, no. 6, pp. 2281–2295, Jun. 2011.

[11] D. Tao, A. P. Doulgeris, and C. Brekke, "Sea clutter contamination test with log-cumulants," in *Proc. SPIE Remote Sensing*, vol. 8536, Edinburgh, UK, Sep. 2012.

[12] N. Balakrishnan and A. Basu, *The Exponential Distribution: Theory, Methods and Applications*. Gordon and Breach Publishers, 1995.

[13] P. McLane, P. Wittke, and C. K.-S. Ip, "Threshold control for automatic detection in radar systems," *Aerospace and Electronic Systems, IEEE Transactions on*, vol. AES-18, no. 2, pp. 242–248, Mar. 1982.

[14] E. Al-Hussaini and B. Ibrahim, "Comparison of adaptive cell-averaging detectors for multiple-target situations," *Communications, Radar and Signal Processing, IEE Proceedings F*, vol. 133, no. 3, pp. 217–223, Jun. 1986.

[15] M. Barkat, S. Himonas, and P. Varshney, "CFAR detection for multiple target situations," *Radar and Signal Processing, IEE Proceedings F*, vol. 136, no. 5, pp. 193–209, Oct. 1989.

[16] S. Himonas and M. Barkat, "Automatic censored CFAR detection for nonhomogeneous environments," *Aerospace and Electronic Systems, IEEE Transactions on*, vol. 28, no. 1, pp. 286–304, Jan. 1992.

[17] G. Trunk, "Range resolution of targets using automatic detectors,"

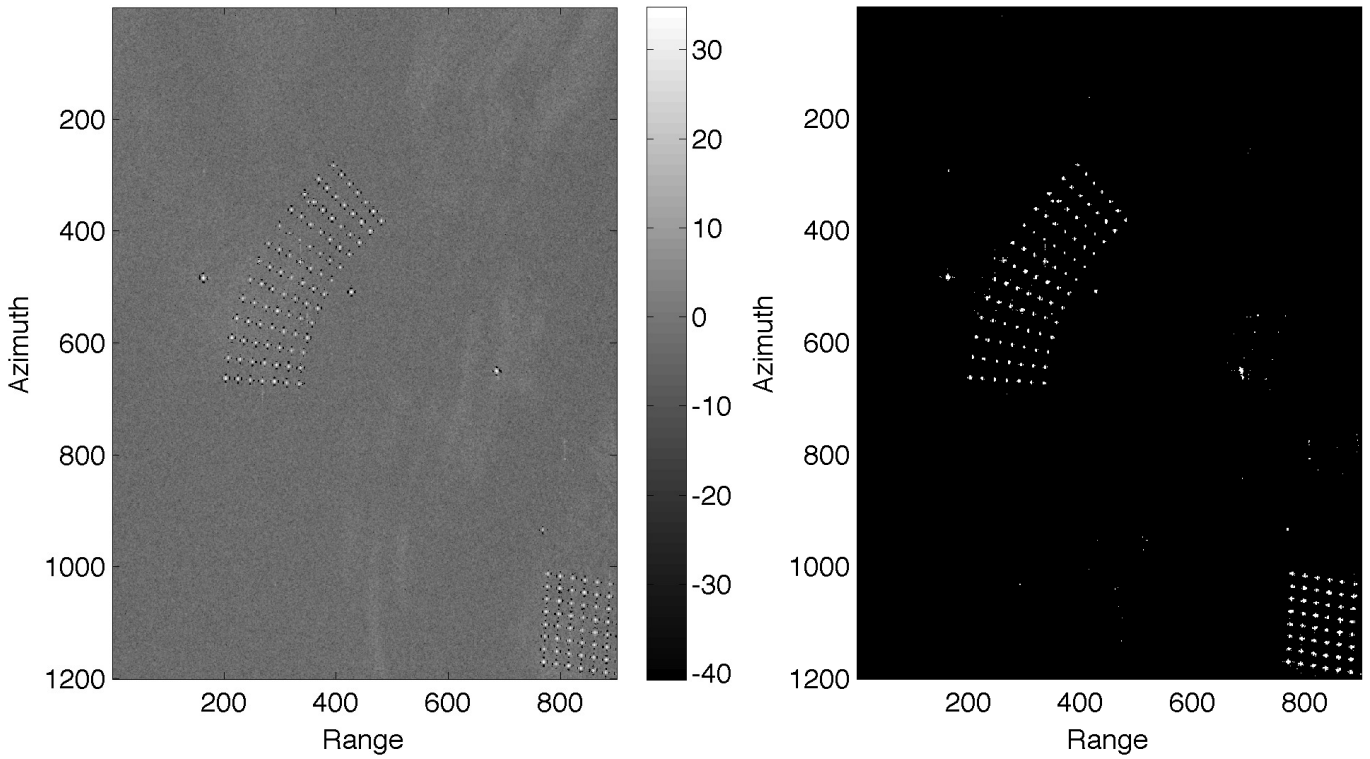

(a) Intensity image in decibels.

(b) Detection result.

Fig. 9. CFAR detection performance study. (a) sub-region of the MLI HH polarization SAR image acquired on 19$^{\text{th}}$ September 2009, offshore of Netherlands (image No.3 in Table I); (b) detection result obtained with 300×300 pixels detection window, 10% truncation ratio, sub-sampling factor 4, 99% confidence level and 0.001% specified false alarm rate.

Aerospace and Electronic Systems, IEEE Transactions on, vol. AES-14, no. 5, pp. 750–755, 1978.

[18] M. Smith and P. Varshney, "Intelligent CFAR processor based on data variability," *Aerospace and Electronic Systems, IEEE Transactions on*, vol. 36, no. 3, pp. 837–847, Jul. 2000.

[19] H. Rohling, "Radar CFAR thresholding in clutter and multiple target situations," *Aerospace and Electronic Systems, IEEE Transactions on*, vol. AES-19, no. 4, pp. 608–621, 1983.

[20] P. Gandhi and S. Kassam, "Analysis of CFAR processors in homogeneous background," *Aerospace and Electronic Systems, IEEE Transactions on*, vol. 24, no. 4, pp. 427–445, 1988.

[21] M. El Mashade, "Monopulse detection analysis of the trimmed mean CFAR processor in nonhomogeneous situations," *Radar, Sonar and Navigation, IEE Proceedings* -, vol. 143, no. 2, pp. 87–94, 1996.

[22] B. Barboy, A. Lomes, and E. Perkalski, "Cell-averaging CFAR for multiple-target situations," *Communications, Radar and Signal Processing, IEE Proceedings F*, vol. 133, no. 2, pp. 176–186, Apr. 1986.

[23] G. Gao, L. Liu, L. Zhao, G. Shi, and G. Kuang, "An adaptive and fast CFAR algorithm based on automatic censoring for target detection in high-resolution SAR images," *Geoscience and Remote Sensing Letters, IEEE*, vol. 47, no. 6, pp. 1685–1697, Jun. 2009.

[24] Y. Cui, G. Zhou, J. Yang, and Y. Yamaguchi, "On the iterative censoring for target detection in SAR images," *Geoscience and Remote Sensing Letters, IEEE*, vol. 8, no. 4, pp. 641–645, Jul. 2011.

[25] J. Rickard and G. Dillard, "Adaptive detection algorithms for multiple-target situations," *Aerospace and Electronic Systems, IEEE Transactions on*, vol. AES-13, no. 4, pp. 338–343, Jul. 1977.

[26] J. Ritcey, "Performance analysis of the censored mean-level detector," *Aerospace and Electronic Systems, IEEE Transactions on*, vol. AES-22, no. 4, pp. 443–454, Jul. 1986.

[27] S. Himonas, "Adaptive censored greatest-of CFAR detection," *Radar and Signal Processing, IEE Proceedings F*, vol. 139, no. 3, pp. 247–255, 1992.

[28] E. Conte, M. Lops, and A. Tulino, "Hybrid procedure for CFAR in non-Gaussian clutter," *Radar, Sonar and Navigation, IEE Proceedings* -, vol. 144, no. 6, pp. 361–369, 1997.

[29] P. Tsakalides, F. Trinic, and C. Nikias, "Performance assessment of CFAR processors in pearson-distributed clutter," *Aerospace and Electronic Systems, IEEE Transactions on*, vol. 36, no. 4, pp. 1377–1386, Oct. 2000.

[30] A. Farrouki and M. Barkat, "Automatic censoring CFAR detector based on ordered data variability for nonhomogeneous environments," *Radar, Sonar and Navigation, IEE Proceedings* -, vol. 152, no. 1, pp. 43–51, Feb. 2005.

[31] S. Blake, "OS-CFAR theory for multiple targets and nonuniform clutter," *Aerospace and Electronic Systems, IEEE Transactions on*, vol. 24, no. 6, pp. 785–790, Nov. 1988.

[32] P. Lombardo and M. Sciotti, "Segmentation-based technique for ship detection in SAR images," *Radar, Sonar and Navigation, IEE Proceedings* -, vol. 148, no. 3, pp. 147–159, Jun. 2001.

[33] V. Hansen and J. Sawyers, "Detectability loss due to "Greatest Of" selection in a cell-averaging CFAR," *Aerospace and Electronic Systems, IEEE Transactions on*, vol. AES-16, no. 1, pp. 115–118, 1980.

[34] E. Al-Hussaini, "Performance of the greater-of and censored greater-of detectors in multiple target environments," *Radar and Signal Processing, IEE Proceedings F*, vol. 135, no. 3, pp. 193–198, Jun. 1988.

[35] B. Chen, P. Varshney, and J. Michels, "Adaptive CFAR detection for clutter-edge heterogeneity using Bayesian inference," *Aerospace and Electronic Systems, IEEE Transactions on*, vol. 39, no. 4, pp. 1462–1470, Oct. 2003.

[36] E. Magraner, N. Bertaux, and P. Refregier, "Detection in gamma-distributed nonhomogeneous backgrounds," *Aerospace and Electronic Systems, IEEE Transactions on*, vol. 46, no. 3, pp. 1127–1139, 2010.

[37] A. Pourmottaghi, M. Taban, and S. Gazor, "A CFAR detector in a nonhomogenous Weibull clutter," *Aerospace and Electronic Systems, IEEE Transactions on*, vol. 48, no. 2, pp. 1747–1758, Apr. 2012.

[38] M. Sciotti and P. Lombardo, "Ship detection in SAR images: a segmentation-based approach," in *Radar Conference, 2001. Proceedings of the 2001 IEEE*, 2001, pp. 81–86.

[39] A. P. Dempster, N. M. Laird, and D. B. Rubin, "Maximum likelihood from incomplete data via the EM algorithm," *Journal of the Royal Statistical Society*, vol. 39, no. 10, pp. 1–38, 1977.

[40] S. N. Anfinsen, A. P. Doulgeris, and T. Eltoft, "Estimation of the equivalent number of looks in polarimetric synthetic aperture radar

imagery," *Geoscience and Remote Sensing, IEEE Transactions on*, vol. 47, no. 11, pp. 3795–3809, Nov. 2009.
[41] ——, "A relaxed Wishart model for polarimetric SAR data," in *Proc. POLinSAR 2009*, Frascati, Italy, Jan. 2009.
[42] J. Lee, D. Schuler, R. Lang, and K. Ranson, "K-distribution for multi-look processed polarimetric SAR imagery," in *Geoscience and Remote Sensing Symposium, 1994. IGARSS '94. Surface and Atmospheric Remote Sensing: Technologies, Data Analysis and Interpretation., International*, vol. 4, Aug. 1994, pp. 2179–2181.
[43] I. G. Cumming and F. H. Wong, *Digital processing of synthetic aperture radar data : algorithms and implementation*, ser. Artech House remote sensing library. Boston: Artech House, 2005.
[44] A. Frery, A. Correia, and C. da Freitas, "Classifying multifrequency fully polarimetric imagery with multiple sources of statistical evidence and contextual information," *Geoscience and Remote Sensing, IEEE Transactions on*, vol. 45, no. 10, pp. 3098–3109, Oct. 2007.
[45] R. Larsen and M. Marx, *An Introduction to Mathematical Statistics and Its Applications*, 5th ed. Prentice-Hall, Incorporated, 2011.
[46] A. Farina, F. Gini, M. Greco, and L. Verrazzani, "High resolution sea clutter data: statistical analysis of recorded live data," *Radar, Sonar and Navigation, IEE Proceedings -*, vol. 144, no. 3, pp. 121–130, Jun. 1997.
[47] D. Iskander and A. Zoubir, "Estimation of the parameters of the K-distribution using higher order and fractional moments," *Aerospace and Electronic Systems, IEEE Transactions on*, vol. 35, no. 4, pp. 1453–1457, Oct. 1999.
[48] S. N. Anfinsen, "On the supremacy of logging," in *Proc. POLinSAR 2011*, Frascati, Italy, Jan. 2011, p. 8.

Ding Tao received the B.E. degree in detection, guidance and control technology from the School of Astronautic at Beijing University of Aeronautics & Astronautics, China, in 2007, and the M.Sc. degree in remote sensing from the Department of Radio and Space Science at Chalmers University of Technology, Gothenburg, Sweden, in May 2010. He started as a Ph.D. student research fellow at the Department of Physics and Technology at the University of Tromsø – The Arctic University of Norway in August 2010, and is also affiliated with the Earth Observation Laboratory and the Barents Remote Sensing School. His current research interests focus on investigating remote sensing, maritime target detection and statistical analysis of sea clutter, in particular with polarimetric synthetic aperture radar images.

Anthony P. Doulgeris (S06M12) received the B.Sc. degree in physics from The Australian National University, Canberra, Australia, in 1988, the M.Sc. degree and the Ph.D. degree in physics from the Department of Physics and Technology, University of Tromsø, Tromsø, Norway, in 2006, and 2011, respectively.

He joined the Department of Physics and Technology at the University of Tromsø – The Arctic University of Norway, in 2007 and is currently an associate professor in applied Earth observation. His research interests focus on investigating remote sensing, pattern recognition and multidimensional statistical modeling, in particular with polarimetric synthetic aperture radar images.

Camilla Brekke (M12) received the Cand. Scient. and Ph.D. degrees from Department of Informatics, University of Oslo, Norway, in 2001 and 2008, respectively. In 2009, she joined the Department of Physics and Technology at University of Tromsø – The Arctic University of Norway as an Associate Professor. She is with the Earth Observation Laboratory and the Barents Remote Sensing School. Her current research interests cover signal and image processing of synthetic aperture radar (SAR) data for arctic and marine applications. In 2001, she was a System Developer with Ericsson, Asker, Norway. From 2001 to 2002, she was a Young Graduate Trainee with the European Space Agency (ESA), Noordwijk, Netherlands. From 2002 to 2009, she was a Scientist with the Norwegian Defense Research Establishment (FFI), Kjeller, Norway.